

Well-defined diatomic catalysis for photosynthesis of C₂H₄ from CO₂

Received: 2 November 2023

Accepted: 4 March 2024

Published online: 18 March 2024

Check for updates

Zhongkai Xie¹, Shengjie Xu¹, Longhua Li¹, Shanhe Gong¹, Xiaojie Wu¹, Dongbo Xu¹, Baodong Mao¹, Ting Zhou¹, Min Chen¹, Xiao Wang², Weidong Shi¹✉ & Shuyan Song²✉

Owing to the specific electronic-redistribution and spatial proximity, diatomic catalysts (DACs) have been identified as principal interest for efficient photoconversion of CO₂ into C₂H₄. However, the predominant bottom-up strategy for DACs synthesis has critically constrained the development of highly ordered DACs due to the random distribution of heteronuclear atoms, which hinders the optimization of catalytic performance and the exploration of actual reaction mechanism. Here, an up-bottom ion-cutting architecture is proposed to fabricate the well-defined DACs, and the superior spatial proximity of CuAu diatomics (DAs) decorated TiO₂ (CuAu-DAs-TiO₂) is successfully constructed due to the compact heteroatomic spacing (2–3 Å). Owing to the profoundly low C–C coupling energy barrier of CuAu-DAs-TiO₂, a considerable C₂H₄ production with superior sustainability is achieved. Our discovery inspires a novel up-bottom strategy for the fabrication of well-defined DACs to motivate optimization of catalytic performance and distinct deduction of heteroatom synergistically catalytic mechanism.

Photocatalytic carbon dioxide (CO₂) reduction, a mimicking natural photosynthesis, is identified as an ideal technology to reduce the CO₂ level by the conversion of CO₂ into fuels or industrial feedstocks with the utilization of solar energy^{1–3}. Among all the photoreduction CO₂ products, ethylene (C₂H₄) is considered as high-value species due to their high energy densities and commercial prices in chemical industry^{4–13}. Bimetallic solid-photocatalysts, consisted of ordered stagger of heteronuclear metal atoms, can strikingly reduce C–C coupling energy barrier via weakening dipole-dipole repulsion of the neighboring adsorbed C-based intermediates, which has been regarded as the dominator in photosynthesis of C₂H₄^{14–21}. Nevertheless, the compact atom stacking during the synthesis of bimetallic solid catalysts inevitably contributes to the decrease of active sites^{22–27}, critically restricting the efficient C₂H₄ generation. Therefore, its deep desirability to accurately optimize bimetallic solid catalysts at the atomic scale to break the bottleneck of inherent scaling-catalytic relationship in photosynthesis of C₂H₄.

Single-atom catalysts (SACs), a well-defined mononuclear metal sites, which have attracted huge attention for their potential to overcome the disadvantages of previously developed solid catalysts²⁷. Conspicuously, heteronuclear DACs can not only maintain the maximized atom utilization but also modulate the reaction kinetics and even the reaction pathways by involving two metal atoms with cooperative modification of their steric and electronic properties^{26–31}. So far, all reported heteronuclear DACs fabrication have concentrated on bottom-up synthetic strategies, such as organometallic compounds pyrolysis^{26,32–35}, metal complexation^{36–38}, metal coprecipitation^{39–43}, in situ photoreduction^{44,45}, and physical desorption^{46,47}. Because of the repellency between the bare metal atoms under such prevailing bottom-up synthesis methods, disordered heteronuclear sites distribution have been an insurmountable barrier, which directly restrained the optimization of catalytic performance and distinct deduction of catalytic mechanisms⁴⁸. Consequently, it is of high priority to exploit novel strategy for well-defined heteronuclear DACs

¹School of Chemistry and Chemical Engineering, Jiangsu University, Zhenjiang 212013, China. ²State Key Laboratory of Rare Earth Resource Utilization, Changchun Institute of Applied Chemistry, Chinese Academy of Sciences, Changchun 130022, China. ✉e-mail: swd1978@ujss.edu.cn; songsy@ciac.ac.cn

fabrication to establish a high-efficiency photosynthesis of C_2H_4 system.

Here, an up-bottom ion-cutting engineering for the synthesis of atomic-level catalysts was initially proposed. Depending on the vectored etching of Cu in a CuAu alloy (isolated Au atoms in the Cu lattice), the CuAu-DAs with subnanometer heteroatomic spacing supported by commercial TiO_2 (CuAu-DAs- TiO_2) were successfully fabricated. The C_2H_4 production of CuAu-DAs- TiO_2 proceeded at a remarkable rate of $568.8 \mu\text{mol}\cdot\text{g}^{-1}\cdot\text{h}^{-1}$ without any sacrificial agent, which is superior to recent reported works in photoconversion CO_2 and H_2O into C_2H_4 (Supplementary Table 1), and no apparent catalyst deactivation was observed during the 120-h photocatalytic stability test. In such CuAu-DAs structures, Cu single atoms (Cu-SAs) are mainly responsible for the high-efficiency *CO generation rather than C-C coupling centers^{16,17,49–52}, while Au single atoms (Au-SAs) serve as *CO coupling centers to rapidly consume the *CO arising from Cu-SAs according to photocatalytic CO_2 reduction, which synergistically promotes the high efficiency and sustainability of photoconversion of CO_2 into C_2H_4 ⁵³.

Results

Catalyst synthesis and structural characterization

Compared to the widespread bottom-up synthetic strategies of SACs and DACs^{32–48,50–58}, the up-bottom ion-cutting architecture controlled by the vectored etching of specific element contents in the alloy may provide novel insight for the adjustable design of SACs and DACs.

Figure 1a illustrates the ion-cutting architecture fabrication of Cu nanoclusters (Cu-NCs) decorated Au-SAs (CuAu-NCSAs), CuAu-DAs, and Au-SAs/Cu-SAs supported by TiO_2 via adjusting the vectored etching time of the Cu_5Au_1 alloy. Transmission electron microscopy (TEM) and aberration-correction high-angle dark-field scanning transmission electron microscopy (AC-HAADF-STEM) were carried out to acquire a more spatially resolved structural configuration during the different catalyst synthesis processes. In Supplementary Figs. 1 and 2, the commercial TiO_2 displays the irregular nanoparticle morphology with the ca. 13.6 nm of particle size, and the EDS mapping analysis also verifies the uniform Ti and O elements distribution. Compared to commercial TiO_2 , the regular and larger size of Cu_5Au_1 alloy was observed in Supplementary Fig. 3a, and the compactly connected heterointerface was observed between Cu_5Au_1 and TiO_2 (Supplementary Fig. 3b). In addition, the overlapping Cu and Au elements distribution were also exhibited in EDS mapping images, indicating the successful construction of CuAu alloy (Supplementary Fig. 3c–g). As shown in Fig. 1b and Supplementary Fig. 4, the ordered stagger of Cu/Au atoms stacked Cu_5Au_1 alloy nanoparticles are successfully loaded on bulk commercial TiO_2 , and the isolated Au single atom in Cu lattice provided the precondition for CuAu-DAs formation. Moreover, the 4.43 and 1.71 Å of Au–Au and Cu–Au atomic distance further verify the isolated Au SAs surrounded by Cu atoms rather than the Au atoms in Cu_5Au_1 alloy (Supplementary Fig. 4a–c). After 1 h of vectored etching of Cu atoms (Fig. 1c and Supplementary Fig. 5a–d), slightly destroyed lattice and few Cu vacancies in the Cu_5Au_1 alloy were observed due to

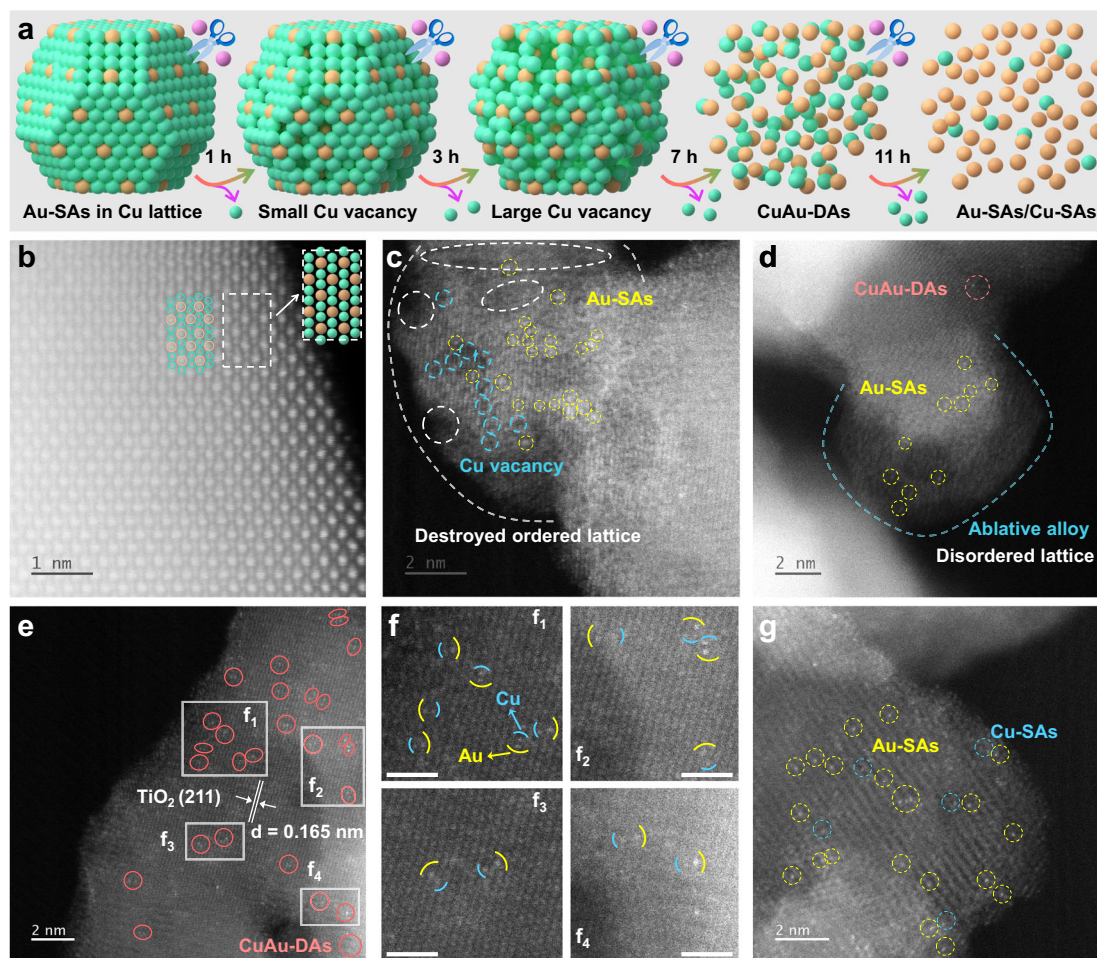


Fig. 1 | Morphological characterization of the CuAu-based TiO_2 composites. a Dynamic schematic illustration from isolated Au-SAs in the Cu lattice to CuAu-DAs during the vectored etching process (green sphere: Cu^0 ; orange sphere: Au^0 ; purple

sphere: Fe^{3+}). AC-HAADF-STEM images of $Cu_5Au_1-TiO_2$ (b), $E_1-Cu_5Au_1-TiO_2$ (c), $E_3-Cu_5Au_1-TiO_2$ (d), $E_7-Cu_5Au_1-TiO_2$ (e), and $E_{11}-Cu_5Au_1-TiO_2$ (g). f Magnified images of the corresponding areas in image (e). Scale bars of f_1 – f_4 : 1 nm.

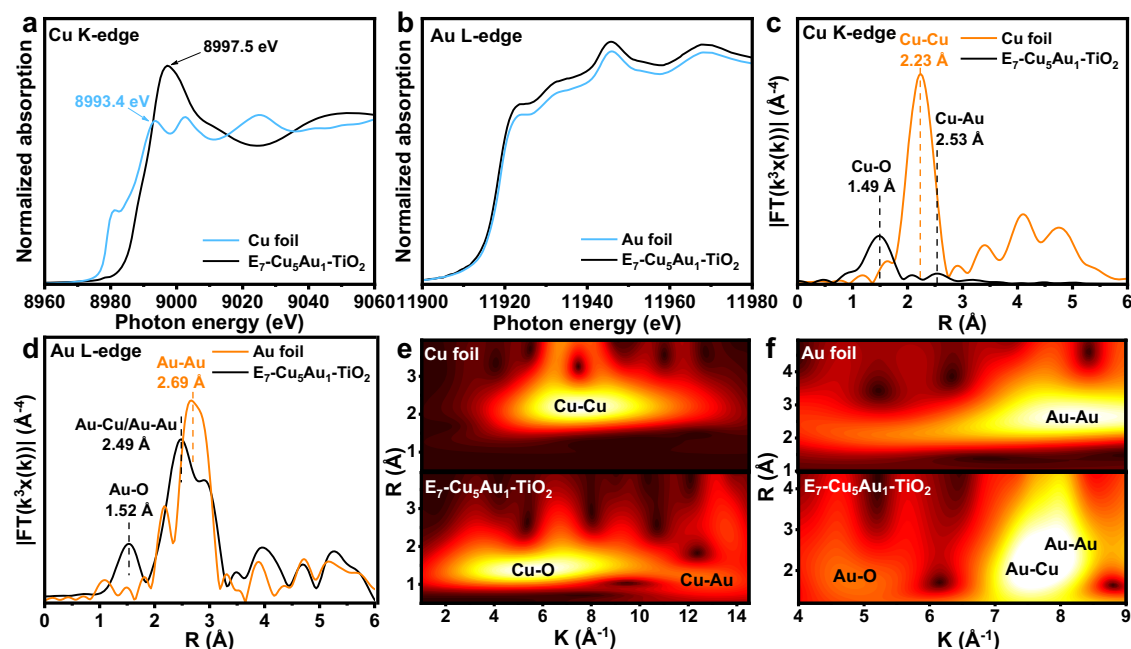


Fig. 2 | Structural characterization of the CuAu-DAs. XANES analysis of $E_7\text{-Cu}_5\text{Au}_1\text{-TiO}_2$ and reference samples at the Cu K-edge (a) and Au L-edge (b). Corresponding k^3 -weighted FT-EXAFS spectra in the R space for $E_7\text{-Cu}_5\text{Au}_1\text{-TiO}_2$

and references at the Cu K-edge (c) and Au L-edge (d). e Cu K-edge WT-EXAFS spectra of Cu foil and $E_7\text{-Cu}_5\text{Au}_1\text{-TiO}_2$. f Au L-edge WT-EXAFS spectra of Au foil and $E_7\text{-Cu}_5\text{Au}_1\text{-TiO}_2$.

the destruction of the ordered arrangement of Cu-Au atoms. The ablative Cu_5Au_1 alloy and few CuAu-DAs were obtained after 3 h of etching (Fig. 1d and Supplementary Fig. 6a, b), indicating that the constant loss of Cu atoms could promote the collapse of the Cu_5Au_1 alloy framework and the redistribution of adjacent Cu-Au atoms on the TiO_2 surface. Moreover, the distinguished ordered lattice of TiO_2 and disordered lattice of Cu_5Au_1 were simultaneously observed in HRTEM and the corresponding pseudo-color images, which further implied the successfully vectored etching of such Cu_5Au_1 alloy (Supplementary Fig. 6c, d). As shown in Fig. 1e, the CuAu-DAs are uniformly dispersed on the surface of the TiO_2 (211) plane (lattice spacing: 0.165 nm) in $E_7\text{-Cu}_5\text{Au}_1\text{-TiO}_2$. In addition, the magnified images (Fig. 1f₁-f₄) and acquired AC-HAADF-STEM image intensity profile (Supplementary Fig. 7) clearly verified subnanometer distances (~2–3 Å) between the Cu-SAs (dark) and Au-SAs (bright) according to the different atomic mass of the corresponding elements⁵⁹, suggesting that the twin CuAu-DAs was successfully constructed after 7 h of vectored etching of the Cu_5Au_1 alloy. Moreover, when the vectored etching time was prolonged to 11 h (Fig. 1g and Supplementary Fig. 8), a few Cu-SAs and dominated Au-SAs were observed in the AC-HAADF-STEM image, indicating that the dynamic vectored etching process promoted the further dissociation of CuAu-DAs structure due to the consistent decrease of Cu atoms. In Supplementary Fig. 9, Cu-SAs modified TiO_2 was also constructed by 7 h of vectored etching of Cu- TiO_2 , suggesting the huge potential of such up-bottom ion-cutting technology for atomic-level catalysts design.

To further investigate the atomic-scale configuration of Cu and Au in $E_7\text{-Cu}_5\text{Au}_1\text{-TiO}_2$, Cu K-edge and Au L-edge X-ray absorption near-edge structure (XANES) spectroscopy was performed (Fig. 2a, b). Figure 2a illustrates the Cu K-edge XANES spectra for $E_7\text{-Cu}_5\text{Au}_1\text{-TiO}_2$ with Cu foil benchmarks as reference, and the absorption edge position of $E_7\text{-Cu}_5\text{Au}_1\text{-TiO}_2$ is more positive than that of Cu foil, indicating that partial Cu could directly connect with the lattice O of TiO_2 . In Fig. 2b, the white line peak of $E_7\text{-Cu}_5\text{Au}_1\text{-TiO}_2$ exhibits Au characteristic features, which is similar to those of the reference Au foil, indicating the presence of Au^0 . As shown in Fig. 2c, the local coordination around the Cu-O shell and Cu-M shell (Cu-Cu and Cu-Au) was determined by

the k^3 -weighted Fourier transform of the extended X-ray absorption fine structure (FT-EXAFS) spectrum. A predominant peak at -1.49 Å of $E_7\text{-Cu}_5\text{Au}_1\text{-TiO}_2$ is assigned to the Cu-O coordination. Furthermore, the other obvious characteristic peak at -2.53 Å is observed in the $E_7\text{-Cu}_5\text{Au}_1\text{-TiO}_2$ spectrum but not in the Cu foil spectrum, implying the possible formation of Cu-Au coordination. The local peak at -1.52 Å in the Au L-edge spectrum of CuAu-DAs- TiO_2 (Fig. 2d) is close to that of Au-O, indicating the formation of Au-O coordination. An apparent path at -2.49 Å is observed in the Au L-edge spectrum of $E_7\text{-Cu}_5\text{Au}_1\text{-TiO}_2$ (Fig. 2d), which is close to the values of Cu-Au and Au-Au (Fig. 2c). The Cu foil is used to calculate the standard amplitude reduction factor ($S_0^2 = 0.845$, Supplementary Table 2), and the Cu K-edge EXAFS analysis of $E_7\text{-Cu}_5\text{Au}_1\text{-TiO}_2$ in R spaces is exhibited in Supplementary Fig. 10. The EXAFS spectrum of $E_7\text{-Cu}_5\text{Au}_1\text{-TiO}_2$ is analyzed by using two backscattering paths (Cu-O and Cu-Au). The best-fitting results exhibited that the coordination number of the O and Au in the first coordination sphere of $E_7\text{-Cu}_5\text{Au}_1\text{-TiO}_2$ is fitted to be ≈ 3.3 and ≈ 1.2 at distances of 1.93 and 2.91 Å, respectively, implying the Cu-SAs is merely adjacent with single Au atom. Therefore, there is no doubt that the existence of CuAu-DAs structure under such vectored etching process, while it is still recognized indeed small existence of pure Au phase due to the shortage of such solvothermal method for the fabrication of highly ordered CuAu alloy. Moreover, the concurrent detection of Cu-M and Au-M distances is in the range of the observed distribution of twin dual atoms in atomic-resolution STEM imaging (Supplementary Fig. 7), further demonstrating that the Cu-Au bond originated from the initial CuAu alloy rather than from Cu-SAs and Au-SAs rearrangement during the etching process. The Cu K-edge and Au L-edge EXAFS oscillations are also analyzed by the wavelet transform (WT) method to further confirm the presence of the Cu-Au path. No WT maxima at 7.5 \AA^{-1} (Cu-Cu bond) and 8.3 \AA^{-1} (Au-Au bond) were observed in the spectra of $E_7\text{-Cu}_5\text{Au}_1\text{-TiO}_2$ (Fig. 2e, f), indicating the SAs-structure configuration of most Cu and Au sites. The WT maxima at 5.7 \AA^{-1} and 13 \AA^{-1} in the spectra of $E_7\text{-Cu}_5\text{Au}_1\text{-TiO}_2$ correspond to the Cu-O and Cu-Au bonds, respectively (Fig. 2e). Similarly, the WT maxima at 4.9 \AA^{-1} and 7.7 \AA^{-1} are attributed to the Au-O and Au-Cu/Au-Au bonds (Fig. 2f), respectively, consistent with the FT-EXAFS results (Fig. 2c, d).

Consequently, the adjacent Cu and Au coexisted as twin diatomic centers and connected with the lattice O of TiO₂ to form O-Cu-Au-O.

As shown in Supplementary Fig. 11a, the Cu 2p X-ray photoelectron spectroscopy (XPS) binding energy peaks at approximately 932.23 and 952.03 eV are attributed to Cu⁰/Cu⁺⁶⁰. The Auger electron spectrum (Cu LMM) was obtained to further distinguish between Cu⁰ and Cu⁺ in Cu-TiO₂ and Cu₅Au₁-TiO₂. As shown in Supplementary Fig. 12, the characteristic kinetic energy peaks at 918.06 and 921.82 eV⁶¹ have corresponded to the electron state of Cu⁰ in Cu-TiO₂ and Cu₅Au₁-TiO₂. The presence of weak peaks located at 934.70 and 954.40 eV confirms the presence of trace Cu²⁺ in Cu-TiO₂ and Cu₅Au₁-TiO₂. Notably, no Cu⁰ or Cu²⁺ were detected in E₇-Cu₅Au₁-TiO₂ because Cu was below the detection limits after the cooperative Fe³⁺ and H⁺ etching reaction of Cu⁰ and Cu²⁺, consistent with the rare residual Cu-SAs observed in AC-HAADF-STEM (Fig. 1e). In Supplementary Fig. 11b, the two Au 4f peaks of Au-TiO₂ located at 82.99 (Au 4f_{7/2}) and 86.70 eV (Au 4f_{5/2}) are attributed to zero valence Au. Compared to those of Au-TiO₂, the Au 4f_{7/2} and Au 4f_{5/2} characteristic peaks of Au₅Cu₁-TiO₂ are positively shifted to 83.18 and 86.90 eV, indicating the impeded electron transfer from TiO₂ to Au due to the surrounding Cu barrier. After the etching process, the Au 4f binding energy peaks of E₇-Cu₅Au₁-TiO₂ are more negative than those of Au-TiO₂ and Cu₅Au₁-TiO₂, illustrating that more TiO₂ local electrons are transferred to Au due to the decreased amounts of Cu, further suggesting the direct concatenation between Au and Cu. The most negative Au 4f binding energies of E₇-Cu₅Au₁-TiO₂ suggest the high-concentration electron density of Au, which inevitably benefits the multiple electron reaction conduction on the Au sites. Consequently, large amounts of photogenerated electrons may be transferred from TiO₂ to the CuAu-DAs due to the low Fermi level of metallic Cu and Au^{62,63}, which may cause both Cu-SAs and Au-SAs to be the main centers for CO₂ adsorption-activation and C-C coupling. Significantly, the Ti 2p spectra of E₇-Cu₅Au₁-TiO₂ exhibits peaks of Ti 2p_{3/2} and Ti 2p_{1/2} at more negative binding energies compared to those of Cu-TiO₂, Au-TiO₂, and Cu₅Au₁-TiO₂ (Supplementary Fig. 11c), further indicating that the Cu-SAs and Au-SAs are more beneficial for photogenerated electron migration from TiO₂ to the CuAu-DAs under irradiation. All the O 1s spectra of the as-prepared samples show two typical peaks, which are assigned to the O-Ti bond of TiO₂ and the O-H bond of surface adsorbed OH groups⁶² (Supplementary Fig. 11d). X-ray diffraction (XRD) was conducted to further analyze the crystal surface information of these TiO₂-based samples. Compared to anatase TiO₂ (JCPDS No. 71-1166), the as-prepared Au-TiO₂ and Cu₅Au₁-TiO₂ composites gives rise to (200), (220), and (311) characteristic peaks of Au (JCPDS 65-2870), while no characteristic peak of Cu was observed in Cu₅Au₁-TiO₂ and Cu-TiO₂ (Supplementary Fig. 13), indicating the rapid growth of pure Au phase and the restrained ordered growth of Cu in the CuAu structure due to the different standard electrode potential (*E*⁰) of Au ([AuCl₄]/Au⁰, *E*⁰ = +0.93 V) and Cu (Cu²⁺/Cu⁰, *E*⁰ = +0.34 V)⁶⁴. Notably, the HRTEM and EDS mapping images exhibited the small-sized Cu nanoparticle (ca. 7.9 nm) decorated TiO₂ (Supplementary Fig. 14a–d), and the EDS mapping also showed the uniformly dispersed Cu elements (Supplementary Figs. 14 and 15), which indicated that Cu existed as the small-sized scale rather than extended growth into large-sized structure (Supplementary Fig. 14e–h). There has been reported that the low ordering degree of CuAu alloy merely display the Au characteristic peaks due to the dominated Miller indexes of Au phase⁶⁵, which is corresponded to the observation of weak Au characteristic peaks in our work. Although the AC-HAADF-STEM and EDS mapping display the Cu atoms surrounded isolated Au single atoms (Supplementary Fig. 4d–g), the predominated 0.233 nm of lattice spacing was observed in the AC-HAADF-STEM of Cu₅Au₁-TiO₂, which is ascribed to the (111) crystal facet of Au rather than Cu and CuAu characteristic lattice planes. Therefore, the apparent characteristic crystal facet of Au that displayed in AC-HAADF-STEM images and XRD reflections could be ascribed to the dominated Miller

indexes of Au phase (Supplementary Figs. 4d and 13). According to the dynamic XRD patterns of Cu₅Au₁-TiO₂ after different vectored etching time (Supplementary Fig. 16a, b), no obvious enhanced Au characteristic peak intensity of E₇-Cu₅Au₁-TiO₂ was observed compared to that of Cu₅Au₁-TiO₂ after the vectored etching process, suggesting that the vectored etching processes of Cu could not promote isolated Au-SAs rearrangement to form Au lattice plane. Inductively coupled plasma-atomic emission spectroscopy (ICP–AES) was conducted to evaluate the dynamic Cu/Au molar ratios during the etching process. In Supplementary Fig. 17, with increasing etching time, the Cu/Au molar ratio value of E₇-Cu₅Au₁-TiO₂ decreases deeply, while the molar ratio values of H₇-Cu₅Au₁-TiO₂ decrease slightly, indicating the presence of large amounts of Cu⁰ rather than Cu⁺/Cu²⁺ and the successful construction of an adjustable CuAu atomic-level nanostructure. Owing to the different redox capacity-related standard electrode potential between Fe³⁺ (Fe³⁺ + e⁻ → Fe²⁺, *E*⁰ = +0.77 V) and Cu⁰ (Cu²⁺ + 2e⁻ → Cu⁰, *E*⁰ = +0.34 V), the Fe³⁺ could spontaneously be reduced by Cu⁰ (Fe³⁺ + Cu⁰ → Fe²⁺ + Cu²⁺)⁶⁴. However, due to the insufficient oxidized capacity of Fe³⁺ for Au⁰ (Au³⁺ + 3e⁻ → Au⁰, *E*⁰ = +1.52 V) oxidation⁶⁴, the contents of Au keep constant during the whole etching process (Supplementary Table 3), which seriously restrains the dissolution of Au⁰ and promote the redistribution of Au atoms on TiO₂. Localized surface plasmon resonance (LSPR) is often related to the metal shape and the dielectric constant of the surrounding medium⁶⁶. Therefore, the connection between atomic interface engineering and the light absorption of the as-prepared samples was also checked by UV–vis–NIR diffuse reflection spectroscopy (DRS). As shown in Supplementary Fig. 18a, an obvious redshift is observed over metal-decorated TiO₂ compared to pure TiO₂, implying that Cu and Au could effectively enhance visible light absorption and produce more photogenerated carriers. In Supplementary Fig. 19a, E₇-Cu₅Au₁-TiO₂ shows strikingly increased Au (~520 nm) and Cu (~730 nm) LSPR response peaks compared to Cu₅Au₁-TiO₂, indicating that the regularly variational nanoscale of Au and Cu can benefit the formation of higher electron density centers upon irradiation. However, with the persistent etching of Cu, the LSPR response of Cu almost disappeared due to the consistently decreased content of Cu. Moreover, H₇-Cu₅Au₁-TiO₂ show much weaker Au LSPR response than E₇-Cu₅Au₁-TiO₂ (Supplementary Fig. 19b, c), and the negligible Cu LSPR response intensity of H₇-Cu₅Au₁-TiO₂ confirms that the H⁺ etching process eliminated only a small amount of surficial oxidized Cu to a certain extent, which implied that E₇-Cu₅Au₁-TiO₂ could induce a higher photogenerated carrier density on CuAu sites due to the stronger Cu and Au LSPR response intensity.

To reveal the charge carrier dynamics on CuAu-DAs modified TiO₂, photoluminescence (PL) spectroscopy and time-resolved photoluminescence (TRPL) spectroscopy were carried out. As shown in Supplementary Fig. 20a, the intensity of the emission peaks of Cu-TiO₂, Cu₅Au₁-TiO₂, and E₇-Cu₅Au₁-TiO₂ at ~425 nm decrease considerably compared to that of pure TiO₂, indicating that the decoration of metallic cocatalysts on TiO₂ can improve the charge separation and transfer. Notably, the spectrum of E₇-Cu₅Au₁-TiO₂ displays a weaker emission peak than that of Cu₅Au₁-TiO₂, indicating the lower photogenerated charge recombination of E₇-Cu₅Au₁-TiO₂ due to the feed-through charge transfer channel between TiO₂ and CuAu-DAs. It is reported that the contributions of τ₁ and τ₂ are more related to charge transfer, and the PL decay is more dominated by τ₃^{67–69}. In Supplementary Fig. 20b and Table 4, the CuAu-DAs modified TiO₂ exhibits shorter τ₁, τ₂, and τ₃ compared to TiO₂, illustrating the compact interaction and suppressed charge recombination between CuAu-DAs and TiO₂. Moreover, the shortest τ₃ lifetime of CuAu-DAs modified TiO₂ represents the fastest decay in CuAu-DAs-TiO₂, which is ascribed to the fact that the direct connection between CuAu-DAs and TiO₂ is more beneficial for convenient photogenerated charge transfer from TiO₂ to CuAu-DAs rather than recombination in the Cu and Cu₅Au₁ bulk. Transient photocurrent and electrochemical impedance

spectroscopy (EIS) measurements were also conducted to further reveal the efficiency of photogenerated charge separation and transportation of the as-synthesized samples. In Supplementary Fig. 20c, d, the highest photocurrent density and smallest arc radius of $E_7\text{-Cu}_5\text{Au}_1\text{-TiO}_2$ suggest that the CuAu-DAs exhibits much higher charge separation efficiency and faster interfacial charge transportation than TiO_2 , Cu-TiO_2 , and $\text{Cu}_5\text{Au}_1\text{-TiO}_2$. Therefore, the superior photoreduction CO_2 performance of CuAu-DAs- TiO_2 could also be attributed to the excellent photoabsorption and high-efficiency charge separation.

Photocatalytic performance toward CO_2 photoreduction

A suitable band edge position of TiO_2 is a prerequisite for the successful photoconversion of CO_2 gas and H_2O vapor into CO , CH_4 , C_2H_4 , C_2H_6 , and O_2 upon 320–780 nm irradiation (Supplementary Fig. 18e). To uncover the influence of different CuAu atomic interfaces on the CO_2 photoreduction reaction, photocatalytic CO_2 reduction tests were carried out on different CuAu nanostructure-decorated TiO_2 samples. At the same loading amounts, Cu-TiO_2 and Au-TiO_2 achieved much higher CO and CH_4 production rates than pure TiO_2 (Fig. 3a and Supplementary Fig. 21a, b) due to the increased number of active sites and the improved charge transfer efficiency⁷⁰. As shown in Fig. 3a and Supplementary Fig. 21a, b, $\text{Cu}_5\text{Au}_1\text{-TiO}_2$ performs a higher CH_4 production rate ($20.4 \mu\text{mol}\cdot\text{g}^{-1}\cdot\text{h}^{-1}$) than Cu-TiO_2 and Au-TiO_2 , which is attributed to the fact that the Au matrix often functions as an electron sink, while the adjacent surficial Cu serves as CO_2 activation centers and proton transfer stations^{70,71}, and the intermediate further combines with the surrounding abundant electrons originating from the Au matrix to promote CH_4 production through the carbene pathway^{62,72,73}. The actual active sites merely exist on the exposed alloy surface rather than in the interior of the bulk, resulting in the catalytic reaction typically occurring on the unsaturated active sites of the CuAu alloy surface. Therefore, photocatalytic CO_2 reduction tests of the etched samples were also performed to further investigate the influence of CuAu interfacial engineering on the photoreduction of CO_2 . In Supplementary Fig. 22, a possible schematic illustration is shown to describe the dynamic change in the CuAu structural configuration

during the constant vectored etching process and define a possible correlation with the photocatalytic performance. With increasing vectored etching time, a peculiar dual volcanic relationship of the hydrocarbon production rate is observed in the $E_7\text{-Cu}_5\text{Au}_1\text{-TiO}_2$ series (Fig. 3b). After 1 h of vectored etching of $\text{Cu}_5\text{Au}_1\text{-TiO}_2$, $E_1\text{-Cu}_5\text{Au}_1\text{-TiO}_2$ reaches the highest CH_4 production (68.2 $\mu\text{mol}\cdot\text{g}^{-1}\cdot\text{h}^{-1}$) and electron-based selectivity (84.7%) among the series of $E_7\text{-Cu}_5\text{Au}_1\text{-TiO}_2$ (Fig. 3b and Supplementary Fig. 21c, d), which is ascribed to the increased number of unsaturated Au and Cu active sites (Supplementary Fig. 22). Nevertheless, the CH_4 production rate continuously decrease due to the constant decrease in the number of Cu atom active sites after a longer vectored etching time. Notably, when the etching time is prolonged to 7 h (Fig. 3b, c and Supplementary Fig. 21c, d), the C_2H_4 and C_2H_6 production rates of $E_7\text{-Cu}_5\text{Au}_1\text{-TiO}_2$ reach 71.6 and 8.5 $\mu\text{mol}\cdot\text{g}^{-1}\cdot\text{h}^{-1}$, respectively, and the electron-based selectivity reached 68.3% (C_2H_4) and 9.4% (C_2H_6). The dramatically increased C_2H_4 production rate of $E_7\text{-Cu}_5\text{Au}_1\text{-TiO}_2$ is 305 and 73 times higher than that of TiO_2 and $\text{Cu}_5\text{Au}_1\text{-TiO}_2$, respectively, which is ascribed to the superior synergistically enhanced C-C coupling over CuAu-DAs. With the further etching of Cu-SAs, the C_2H_4 production rate of $E_9\text{-Cu}_5\text{Au}_1\text{-TiO}_2$ and $E_{11}\text{-Cu}_5\text{Au}_1\text{-TiO}_2$ constantly decrease due to the constantly decreasing amounts of Cu-SAs, implying that the mere presence of Au-SAs (Fig. 1g) could not satisfy the high-efficiency C-C coupling and C_2H_4 production. Moreover, the optimized amount of $E_7\text{-Cu}_5\text{Au}_1\text{-TiO}_2$ photocatalysts was verified to be 20 mg with a highest C_2H_4 production rate based on the excellent mass transfer and superior light utilization (Supplementary Fig. 23), and the apparent decrease of C-based products production rate was observed with the addition of superfluous photocatalysts, which could be ascribed to the impeded light transmission⁷⁴. Compared to Au-SAs modified TiO_2 , Cu-SAs (Supplementary Fig. 9) modified TiO_2 ($E_7\text{-Cu-TiO}_2$) exhibits dramatically increased CO and CH_4 generation, while negligible C_2 generation is also observed on $E_7\text{-Cu-TiO}_2$, indicating that the Cu-SAs is beneficial for high-efficiency CO production (Supplementary Fig. 24), consistent with recent research results on Cu-SAs based photocatalytic CO_2 reduction^{75–79}. Therefore, we suspect that only the specific existence of adjacent Cu-SAs and

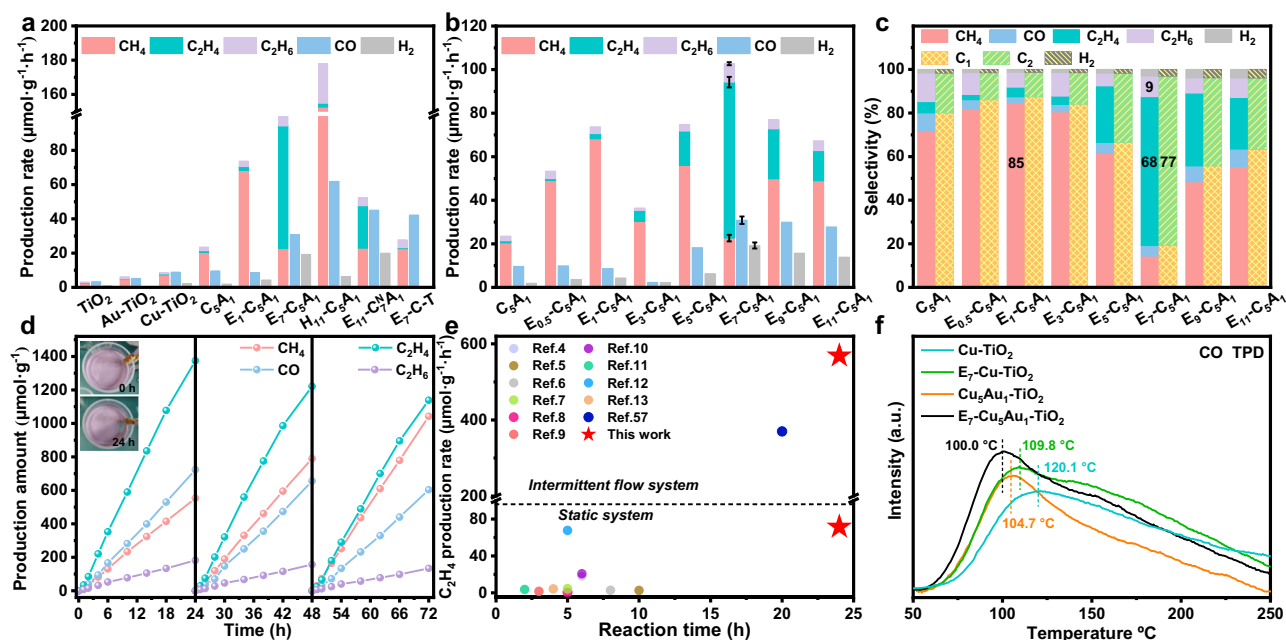


Fig. 3 | Photocatalytic performance of CuAu-based TiO_2 composites. CH_4 , C_2H_4 , C_2H_6 , CO , and H_2 production rates of the as-prepared photocatalysts (a) and $E_7\text{-Cu}_5\text{Au}_1\text{-TiO}_2$ (b). c Electron-based selectivity of photocatalytic CO_2 conversion over $E_7\text{-Cu}_5\text{Au}_1\text{-TiO}_2$. d Long-term photocatalytic stability test of $E_7\text{-Cu}_5\text{Au}_1\text{-TiO}_2$.

e C_2H_4 production rate of $E_7\text{-Cu}_5\text{Au}_1\text{-TiO}_2$ with the reaction time in comparison with recent reports during the closed glass photoreduction of CO_2 with a H_2O gas-circulation system without any sacrificial agents. f CO-TPD profile of the as-prepared samples.

Au-SAs can efficiently and synergistically favor C-C coupling and C₂H₄ production. To further confirm that the CuAu-DAs structure can promote C₂H₄ generation, a photoreduction CO₂ test was also conducted on E₇-Cu₇^NAu₁-TiO₂ (Supplementary Fig. 25) constructed by adding additional Cu content to the Cu₅Au₁ alloy. The dual volcanic relationship of the hydrocarbon production rate is still observed on E₇-Cu₇^NAu₁-TiO₂ based on the transformation of the CuAu structure. Furthermore, E₁₁-Cu₇^NAu₁-TiO₂ exhibits the maximum C₂H₄ production rate after 11 h of vectored etching (Supplementary Fig. 25a), and the CO production also rapidly increase with enhanced C₂H₄ generation, similar to the behavior of E₇-Cu₅Au₁-TiO₂, indicating that the *CO species is a critical intermediate for C-C coupling, as reported^{6,14,53}. As shown in the ICP-AES results (Supplementary Fig. 26 and Table 5), the Cu/Au molar ratios of both E₇-Cu₅Au₁-TiO₂ and E₁₁-Cu₇^NAu₁-TiO₂ are similar, further confirming that the dominated CuAu DAs-structure dramatically actuate C₂H₄ production. Moreover, photoreduction CO₂ tests were also conducted on H₁-Cu₅Au₁-TiO₂ to further identify the effects of different CuAu structures. Although a superior CO production rate (61.8 μmol·g⁻¹·h⁻¹) is observed on H₁₁-Cu₅Au₁-TiO₂ (Supplementary Fig. 27), the C₂ production is still nonideal, emphasizing that only Au-SAs, rather than low-coordination Au sites, could rapidly convert the high-concentration CO into C₂ products. Furthermore, a superhigh CH₄ (152.6 μmol·g⁻¹·h⁻¹) production rate is observed for H₁₁-Cu₅Au₁-TiO₂, indicating that low-coordination Au sites in the Cu lattice are more beneficial for converting *CO into CH₄ than *CO coupling on Au-SAs. Consequently, in such CuAu-DAs modified TiO₂ photocatalytic systems, the Cu-SAs guarantee rapid *CO generation and high-concentration coverage, and the adjacent Au-SAs further promote migration and coupling of the generated *CO. The source of photo-reduced CO₂ products was investigated by using isotope labeling ¹³CO₂ and H₂¹⁸O as the reactant under irradiation, and the products were analyzed by gas chromatography-mass spectrometry (GC-MS). The GC-MS peak sequences of ¹³CO, ¹³CH₄, ¹³C₂H₄, and ¹³C₂H₆ are shown in Supplementary Fig. 28, and the peaks at *m/z* = 29, *m/z* = 17, *m/z* = 30, and *m/z* = 32 are assigned to ¹³CO, ¹³CH₄, ¹³C₂H₄, and ¹³C₂H₆, indicating that the carbon source of CO and hydrocarbons is indeed derived from the input CO₂ gas. Overall CO₂ photoreduction is divided into two major half reaction steps, the CO₂ reduction and H₂O oxidation^{12,80}, and the detection of ¹⁶O¹⁸O and ¹⁸O₂ species verifies that O₂ originates from H₂O oxidation in the photocatalytic CO₂ reduction in (Supplementary Fig. 28). Notably, in Supplementary Fig. 29, O₂ evolution related to holes consumption of the TiO₂ based composites are also stoichiometrically approximate to products of photogenerated electrons reduction, which indicates the simultaneous CO₂ reduction and H₂O oxidation behaviors. The CO₂ photoreduction experiment was also taken under no existence of H₂O to further figure out the influence of H₂O species (Supplementary Fig. 30). No C-based product was detected in the absence of H₂O, indicating the significance of photo-generated holes consumption in the overall CO₂ photoreduction. Therefore, both the investigation of H₂O oxidation and CO₂ reduction are crucial and directive for the development of photocatalysis. Furthermore, a negligible amount of CO production was detected on E₇-Cu₅Au₁-TiO₂ and E₇-Cu₅Au₁-Al₂O₃ upon 420 nm irradiation (Supplementary Fig. 31a), indicating the inappreciable CuAu LSPR effect and the dominant TiO₂ electron donor in photocatalytic CO₂ reduction (Supplementary Fig. 31b). Consequently, the same DAs-modified strategy was conducted on the widespread reported photocatalysts of carbon nitride (C₃N₄) to further verify the universality of such optimized strategy, and the vectored etching Cu₅Au₁ modified C₃N₄ and TiO₂ also exhibit the efficient C₂H₄ production, which sufficiently prove the universality of such CuAu-DAs modification for the optimization of C-C coupling reaction (Supplementary Figs. 32–35).

Cycling tests were performed to analyze the relationship between activity and stability during the photoreduction of CO₂ into C₂H₄ (Fig. 3d). Based on the limitation of catalyst stability, the

majority of photocatalytic CO₂ reduction into C₂H₄ are maintained for only a few hours and accompany with C₂H₄ production stagnation due to the poor structural stability and surface poisoning effect on the photocatalyst (Fig. 3e)^{4–13,57}. As shown in Fig. 3e, regardless of the low-efficiency or high-efficiency C₂H₄ production rate on different photocatalysts, all exhibited limited reaction time due to the deactivation of photocatalysts. Interestingly, in this work, the yield of each product increases linearly during three cycles of 72 h irradiation, as shown in Fig. 3d, and the AC-HAADF-STEM image of E₇-Cu₅Au₁-TiO₂ displays an unchanged CuAu-DAs structural configuration, as shown in Supplementary Fig. 36, indicating the superior structural stability of E₇-Cu₅Au₁-TiO₂ under such high-efficiency C₂H₄ production in the static system. Moreover, compared to the traditional static system, the intermittent flow system is considered a better choice for the improvement of photocatalytic CO₂ reduction due to the high-efficiency transport of mass^{81–86}. Therefore, the intermittent flow system is also adopted to further analyze the stability of photocatalysts under higher efficiency CO₂ conversion circumstances. Notably, in such an intermittent flow system, the C₂H₄ production rate reaches 568.8 μmol·g⁻¹·h⁻¹ (Supplementary Fig. 37a) after 24 h of irradiation, which is superior to those reported in recent works (Fig. 3e). After 5 days of irradiation, C₂H₄ production maintains a rate of 483.2 μmol·g⁻¹·h⁻¹, indicating the superhigh stability of CuAu-DAs catalysts even during such high-efficiency C₂H₄ conversion. In addition, a series of long-term photocatalytic stability tests were carried out on different metallic structure-modified TiO₂ to determine the reason for the superior stability of such specific CuAu-DAs, and CO temperature-programmed desorption (CO-TPD) was also conducted to further analyze the connection between the catalyst structure and CO affinity. As shown in Fig. 3f, Cu-TiO₂ shows the strongest CO adsorption strength centered at -120.1 °C in the weak absorption area compared to other catalysts⁷, indicating that CO desorption is most difficult on this catalyst surface, which may suppress fresh CO₂ adsorption and conversion on Cu-TiO₂ during the photocatalytic CO₂ reduction process. As shown in Supplementary Fig. 38, Cu-TiO₂ also exhibits nonlinear CO generation, which is ascribed to the partially deactivated Cu sites induced by strong CO adsorption. Furthermore, an apparent color change (yellow to black) of Cu-TiO₂ after 24 h of photocatalytic CO₂ reduction is noticed (Supplementary Fig. 38), and the black samples became yellow after 100 °C annealing in a vacuum-treated system (Supplementary Fig. 39), further indicating that the color change could be induced by intermediate adsorption during photocatalytic CO₂ reduction. Furthermore, the possible absorbed isotopically labeled ¹³C intermediates of Cu-TiO₂ after 24 h photocatalytic CO₂ reduction and subsequent 100 °C annealing in a vacuum-treated system were analyzed by GC-MS. The GC-MS peak sequences of ¹³CO are shown in Supplementary Fig. 40, and the peak at *m/z* = 29 is assigned to ¹³CO, indicating the occurrence of CO poisoning on Cu-TiO₂, consistent with the results of the CO-TPD analysis and photocatalytic stability test. However, the CO adsorption strength (109.8 °C) of E₇-Cu-TiO₂ is obviously lower than that of Cu-TiO₂ (Fig. 3f), indicating that the contractible Cu size (nanoparticle to single atom) partially alleviated the CO poisoning effect. Although the CO production of E₇-Cu-TiO₂ increases drastically compared to that of Cu-TiO₂ due to the decreased Cu coordination number, E₇-Cu-TiO₂ still exhibits nonlinear CO generation and a slight color change (white to pale yellow, Supplementary Fig. 41) due to its slight surface CO poisoning (Supplementary Fig. 42), implying that low-coordination-number Cu inevitably suffers CO poisoning. Notably, the CO adsorption strength of Cu₅Au₁-TiO₂ is lower than that of Cu-TiO₂ (Fig. 3f), confirming that the introduction of Au in the Cu lattice weakens the CO adsorption of Cu, as reported⁵³. The linearly increased CH₄

yield (Supplementary Fig. 43) and weakened CO adsorption (Fig. 3f) of Cu₅Au₁-TiO₂ compared to Cu-TiO₂ suggest that the isolated Au in the Cu lattice efficiently promote *CO conversion to CH₄ on the Au sites and suppressed *CO accumulation, which benefits the resistance to catalyst deactivation. However, Cu₅Au₁-TiO₂ also displays a nonlinearly increased CO yield induced by weak CO poisoning due to the large amount of Cu in the Cu₅Au₁ alloy (Supplementary Figs. 43 and 44), which further implies that the addition of Au not only weakens CO adsorption on Cu sites but also serves as a *CO turnover site to rapidly consume the *CO arising from Cu to alleviate the CO poisoning effect on Cu sites. Moreover, the CO-TPD analysis indicates that E₇-Cu₅Au₁-TiO₂ exhibits the highest CO adsorption capacity and lowest CO desorption temperature at -100.0 °C, as shown in Fig. 3f, implying the enormous capacity for CO coverage and the most resistant CO poisoning on CuAu-DAs, which is beneficial for the high efficiency and stability of *CO coupling. Based on the weakest CO chemical adsorption strength of E₇-Cu₅Au₁-TiO₂, no ¹³CO of E₇-Cu₅Au₁-TiO₂ was detected by GC-MS after a 24 h stability test and 100 °C annealing in a vacuum-treated system (Supplementary Fig. 45). Meanwhile, there is also no special characteristic peaks of C-based residual surficial adsorbates was observed in FTIR spectrum after CO₂ photoreduction over E₇-Cu₅Au₁-TiO₂ (Supplementary Fig. 46), suggesting the inexistence of residual C-based intermediate and the superior stability of such CuAu-DAs structure. Owing to the synergistic effect of CuAu-DAs heteronuclear sites, rapid *CO coupling and weakened CO adsorption are simultaneously realized, ensuring superior catalytic sustainability even under such high-efficiency C₂H₄ production.

Mechanism of the photocatalytic performance

Time-dependent in situ diffuse reflectance Fourier transform infrared spectroscopy (DRIFTS) was employed to elucidate the reaction intermediates and concrete evidence of the reaction mechanism under 355 nm laser irradiation for 15 min (Fig. 4a, b). Humid CO₂ was carried into the reaction chamber until equilibrium was reached, and different infrared adsorption characteristic peaks of E₇-Cu₅Au₁-TiO₂ were gradually observed when the photocatalyst was subjected to constant irradiation. As shown in Fig. 4b, monodentate carbonate (m-CO₃²⁻ at 1283 cm⁻¹) and bidentate carbonate (b-CO₃²⁻ at 1688 cm⁻¹) are generated from the co-adsorption of CO₂ and H₂O on the surface of E₇-Cu₅Au₁-TiO₂^{57,87-90}. The peaks at 1670 and 1646 cm⁻¹ are attributed to the vibrations of *CO₂⁻ and *COOH groups^{7,91,92}, respectively. Moreover, the characteristic peak at 1660 cm⁻¹ is assigned to H₂O decomposition signals⁹³, and the constantly increased broad IR bands at 3200–3400 cm⁻¹ are corresponded to the vibration of *OH groups generated from water dissociation under simulated irradiation^{4,6,94}. The different characteristic peaks at approximately 1947 and 2235 cm⁻¹ are assigned to *CO intermediates^{4,7,95}, including Cu-CO and Au-CO on E₇-Cu₅Au₁-TiO₂ (Fig. 4a). Moreover, the contact angles of Cu₅Au₁-TiO₂ and E₇-Cu₅Au₁-TiO₂ are 9° and 7° (Supplementary Fig. 47), respectively, indicating the better surface hydrophilicity of E₇-Cu₅Au₁-TiO₂, which further demonstrates that the low-coordinated Cu and Au atoms are beneficial for H₂O adsorption and the generation of protons to further facilitate the protonation reaction. Coincidentally, asymmetric vibration of *OCCO is observed at -1531 cm⁻¹ (Fig. 4b), providing significant evidence for the C₂ evolution pathway, indicating that the C₂ products arise from the coupling of *CO intermediates^{4,94,96,97}. Moreover, the unique C-C coupling intermediates *C=C (3080 cm⁻¹)⁹⁶, *OCCOH (1579 cm⁻¹)⁶, *OCCHOH (1307 cm⁻¹)⁴, and *C₂H₄ (1447 cm⁻¹)⁶³ were also detected spectroscopically, further indicating the complexly cascaded multiple electron and proton reaction for the ultimate C₂H₄ formation. The vibration frequency of surface-bound *CHO is observed at approximately 1732 and 1710 cm⁻¹ on E₇-Cu₅Au₁-TiO₂ due to the one-electron and one-proton reduced reaction of the *CO

intermediate^{63,96,98}. Additionally, the peaks at approximately 2993, 2944, and 2881 cm⁻¹ are attributed to the C-H symmetric stretching vibrations of methylene (Fig. 4a), facilitating the evolution of CH₄ or C₂H₄ products⁴. The characteristic spectral peaks at approximately 1372, 1474, and 2965 cm⁻¹ are attributed to *CH₂, *CH₂, and *CH₃ intermediates, respectively^{57,99}, demonstrating that these intermediates could be the source of hydrocarbons. Gibbs free energy theoretical calculations were conducted to elucidate the correlation between the specific nanostructure, electronic properties, and catalytic performance. By combining these results with the time-dependent in situ DRIFTS results, these possible reaction pathways were further proposed by Gibbs free energy calculations. In Fig. 4c, the formations of *CO₂, *COOH, and *CO on E₇-Cu₅Au₁-TiO₂ are constantly exothermic and spontaneous processes, indicating that the synergistic effect between Cu-SAs and Au-SAs could significantly promote CO₂ adsorption and activation to produce large amounts of *CO intermediates, which is beneficial for *CO coupling under such high concentrations of *CO. The hydrogenation and desorption of *CO to *CHO and CO species require 1.30 and 1.85 eV of energy expenditure, respectively, while *CO coupling to *OCCO consume only 0.54 eV of energy input. Because the energy barrier of *CO coupling is much lower than that of *CO hydrogenation and desorption, the *OCCO intermediates are confirmed to form preferentially during the *CO transformation process. Furthermore, under the constant hydrogenation process of *OCCO, the C₂H₄ formation paths are theoretically proposed as described in the following formulas: *OCCO → *OCCOH → *OCCHOH → *OCCH → *OCCH₂ → *OHCHCH₂ → *CHCH₂ → C₂H₄. Therefore, the reaction mechanism of photoreduction CO₂ into C₂H₄ is determined in detail on the basis of the time-dependent in situ DRIFTS experiments and density functional theory (DFT) simulations.

Mechanism for the resistance of catalyst deactivation

The enhanced CO poisoning resistance of CuAu hybrid catalysts during photocatalytic CO₂ reduction tests compared to that of pure Cu was considered. DFT calculations of Cu-NCs, Cu-SAs, CuAu alloy, and CuAu-DAs modified TiO₂ models were performed to further analyze the relation between C-based intermediate conversion efficiency and different nanostructures (Fig. 5a). During the *CO generation process, there is almost no energy input for *CO₂, *COOH, and *CO formation in these models (Fig. 5a), which implies rapid *CO formation due to these exothermic and spontaneous processes. Nevertheless, all the conversions from *CO to *CHO, *OCCO, and CO molecules in these models must overcome an enormous energy barrier, indicating the rate-determined significance of *CO conversion during the CO₂ reduction process. During three possible *CO conversion routes (*CO → CO, *CO → *CHO, *CO → *OCCO), the optimized energetically favorable *CO coupling modes could not be formed on Cu-NCs-TiO₂ (C-C distance, 3.68 Å), Cu-SAs-TiO₂ (C-C distance, 2.92 Å), and CuAu-alloy-TiO₂ (C-C distance, 3.76 Å) due to the weak interaction between adjacent adsorbed *CO intermediates (Fig. 5b). In Supplementary Fig. 48, CuAu-DAs-TiO₂ (-1.98 eV) presents the highest *CO adsorption energies compared to CuAu-alloy-TiO₂ (-1.44 eV), Cu-NCs-TiO₂ (-1.55 eV), and Cu-SAs-TiO₂ (-1.79 eV), ensuring the compact *CO interaction and high-concentration *CO coverage¹⁰⁰ (Fig. 5b, C-C distance, 1.40 Å), which contributes to the successful construction of the *OCCO intermediate on CuAu-DAs-TiO₂ due to the optimized surface adsorption configurations resulting from the cooperative modification of the steric and electronic properties of CuAu-DAs^{26,28-31}. Compared to *CO desorption to CO, *CO is preferentially protonated due to the lower energy barrier and energy input for *CHO production on Cu-NCs-TiO₂ (1.15 eV), Cu-SAs-TiO₂ (1.41 eV), and CuAu-alloy-TiO₂ (0.21 eV). Although the transformation of reaction routes could be an efficient way to resist *CO species accumulation, the energy input for *CO conversion to *CHO on Cu-NCs-TiO₂ and Cu-SAs-TiO₂ was still

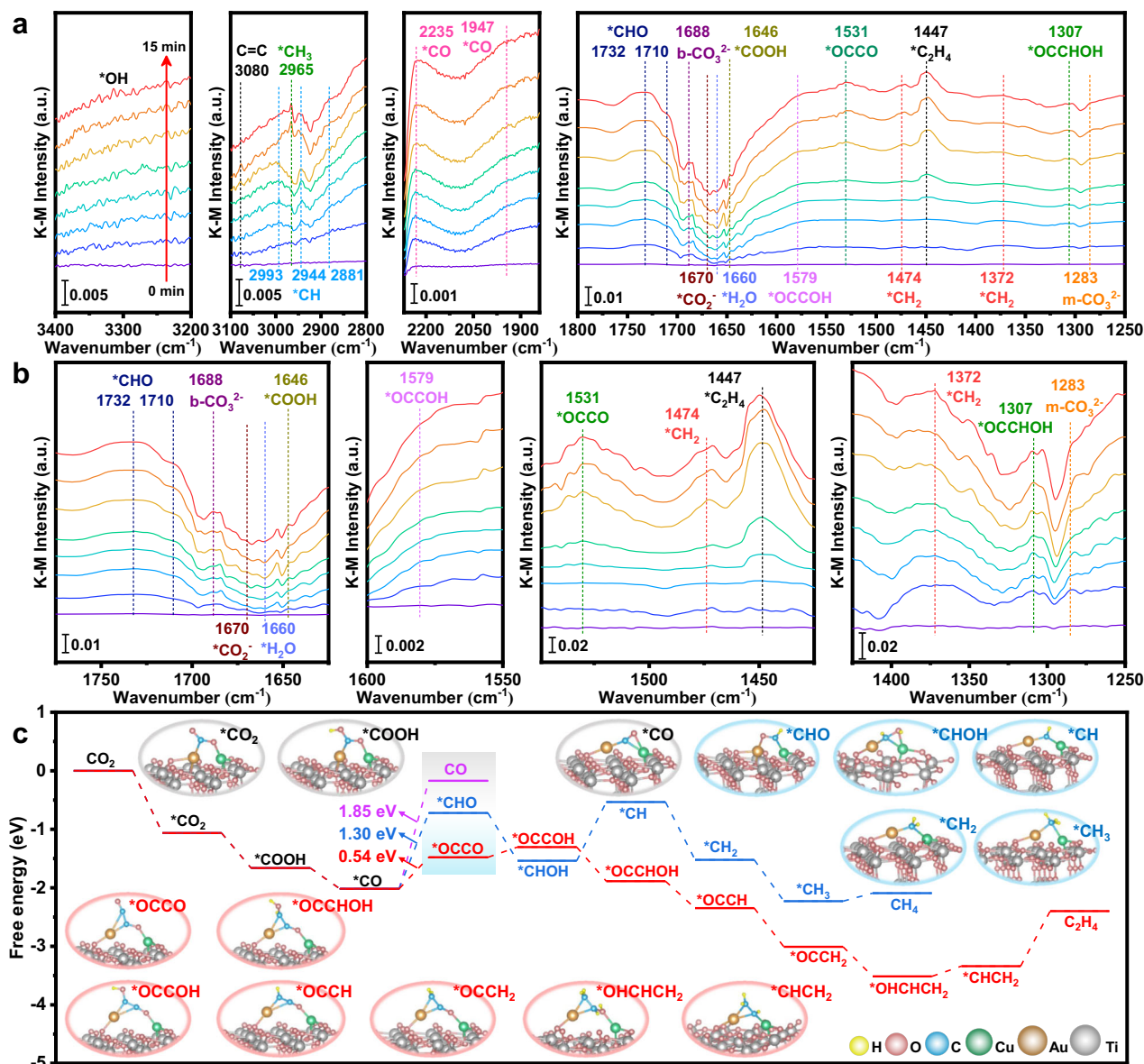


Fig. 4 | Schematics of C₂H₄ generation during photocatalytic CO₂ reduction. **a** In situ DRIFTS detection of E₇-Cu₅Au₁-TiO₂. **b** Corresponding magnifying area of the in situ DRIFTS spectra in **a**. **c** The free energy diagram of CO₂ conversion over

the CuAu-DAS-TiO₂ photocatalyst, together with the atomic structures of the reaction intermediates.

enormous, which also dramatically limited the rapid *CO transformation and led to surface *CO accumulation. Affected by the introduction of Au, the energy input of *CO conversion sharply decreased due to the synergistic cooperation between Cu and Au sites, suggesting that the suppressed *CO poisoning effect could be ascribed to the rapid *CO conversion on CuAu sites^{101,102}. Moreover, the energy input for *CO conversion on CuAu-DAS-TiO₂ (*CO to *OCCO, 0.54 eV) was much lower than that on Cu-SAs-TiO₂ (*CO to *CHO, 1.41 eV) and Cu-NCs-TiO₂ (*CO to *CHO, 1.15 eV), which suggested that the extremely low C-C coupling energy barrier-induced rapid *CO consumption could be the key factor for the sharp *CO poisoning resistance on CuAu-DAS-TiO₂ (Fig. 5a, c). Owing to the synergistic cooperation between the adjacent Cu-SAs and Au-SAs, simultaneous and high-efficiency *CO formation and *CO conversion could be realized based on the reconstituted surface reactant intermediate adsorption configurations and reduced *OCCO coupling reaction energy barrier, which efficaciously overcomes the activity-stability seesaw effect in photoreduction of CO₂ with H₂O into C₂H₄ (Fig. 5c).

Discussion

In summary, CuAu-DAS modified commercial TiO₂ was successfully synthesized by an up-bottom atomic synthetic process involving the vectored etching of Cu atoms in a CuAu alloy. According to the activity tests, CO-TPD, and DFT calculation results of the CuAu-DAS structure, Cu-SAs are beneficial for high-efficiency *CO production, while Au-SAs not only moderate the *CO binding strength of the composites but also strikingly increase the *CO coupling efficiency and suppress catalyst deactivation under high-concentration *CO conditions. Owing to such synergistically catalytic effect of heteronuclear DAS, CuAu-DAS-TiO₂ exhibited a superhigh rate of 568.8 μmol·g⁻¹·h⁻¹ in an intermittent flow system, and the negligible CO poisoning of CuAu-DAS-TiO₂ was observed during the 120-h photocatalytic stability test. Herein, our discovery not only provides a novel insight into the adjustable synthesis of atomic-level catalysts but also provides a new technique to optimize the selectivity, activity, and stability of photocatalysts based on reconstituted surface adsorption configurations of reactant intermediates and reduced reaction barriers.

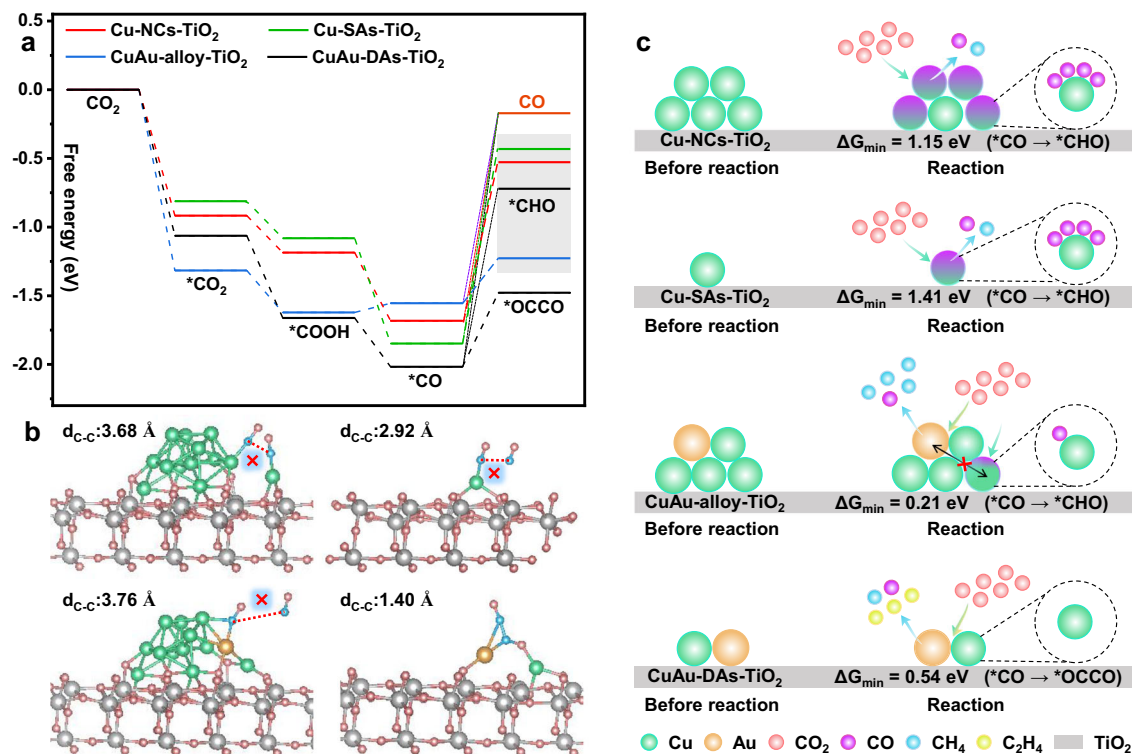


Fig. 5 | Illustration of the model mechanisms. a The free energy diagram of CO₂ reduction to CO, *CHO, and *OCCO over different modeled surfaces. **b** The most energetically favorable *OCCO adsorption configurations. **c** Schematic illustration

of the CO poisoning pathway during the photocatalytic CO₂ reduction reaction on different models.

Methods

Synthesis of Cu₅Au₁-TiO₂

Two hundred milligrams of commercial TiO₂, 105 mg of PVP, 120 mg of L-ascorbic acid, and 300 mg of KBr were dispersed in 8 mL of deionized water, sonicated for 10 min in a 50 mL round-bottom flask, and transferred into an 80 °C oil bath under constant stirring. After 10 minutes of heating, 0.083 mmol of CuCl₂·2H₂O and 0.017 mmol of HAuCl₄·4H₂O were dissolved in 4 mL of H₂O, and the mixed CuCl₂·2H₂O and HAuCl₄·4H₂O solution was rapidly transferred into the round-bottom flask. Finally, the solution was kept at 80 °C for 3 h. The sample was washed with deionized water three times and absolute ethanol three times to remove impurities. The obtained samples were denoted as Cu₅Au₁-TiO₂, which could also be simplified to C₅A₁.

Synthesis of E_t-Cu₅Au₁-TiO₂

FeCl₃·6H₂O (0.06 mmol) was dispersed in 10 mL of 0.1 M HCl, and gaseous Ar was bubbled through the solution for 60 min to eliminate dissolved O₂. Subsequently, 100 mg of Cu₅Au₁-TiO₂ was dissolved into the as-prepared solution. The suspension solution was reacted in an oil bath at 50 °C for different etching reaction time (0.5, 1, 3, 5, 7, 9, and 11 h). The as-prepared samples were washed with 0.1 M HCl and deionized water to remove impurities. The obtained samples were denoted as E_t-Cu₅Au₁-TiO₂ (simplified as E_t-C₅A₁), where t = 0.5, 1, 3, 5, 7, 9, and 11 corresponded to the etching time.

Synthesis of E_t-Cu₇^NAu₁-TiO₂

E_t-Cu₇^NAu₁-TiO₂ was prepared by the same approach as E_t-Cu₅Au₁-TiO₂, except that the amounts of CuCl₂·2H₂O and FeCl₃·6H₂O were 0.119 mmol and 0.084 mmol, respectively. The obtained samples were denoted as E_t-Cu₇^NAu₁-TiO₂ (simplified as E_t-C₇^NA₁), where t = 0.5, 1, 3, 5, 7, 9, 11, and 13 correspond to the etching time.

Synthesis of H_t-Cu₅Au₁-TiO₂

H_t-Cu₅Au₁-TiO₂ was prepared by the same approach as E_t-Cu₅Au₁-TiO₂ without the addition of FeCl₃·6H₂O. The obtained samples were denoted as H_t-Cu₅Au₁-TiO₂ (simplified as H_t-C₅A₁), where t = 0.5, 1, 3, 5, 7, 9, 11, and 13 correspond to the etching time.

Synthesis of Cu-TiO₂

Cu-TiO₂ was prepared by the same approach as Cu₅Au₁-TiO₂ without the addition of HAuCl₄·4H₂O, and the amount of CuCl₂·2H₂O was 0.1 mmol. The obtained sample was denoted as Cu-TiO₂ (C-T).

Synthesis of E_t-Cu-TiO₂

E_t-Cu-TiO₂ was prepared by the same approach as E_t-Cu₅Au₁-TiO₂. The obtained samples were denoted as E_t-Cu-TiO₂ (simplified as E_t-C-T), where t = 0.5, 1, 3, 5, 7, 9, and 11 correspond to the etching time.

Synthesis of Au-TiO₂

Au-TiO₂ was prepared by the same approach as Cu₅Au₁-TiO₂ without the addition of CuCl₂·2H₂O, and the amount of HAuCl₄·4H₂O was 0.1 mmol. The obtained sample was denoted as Au-TiO₂ (simplified as A-T).

Synthesis of E₇-Cu₅Au₁-Al₂O₃

Cu₅Au₁-Al₂O₃ was prepared by the same approach as E₇-Cu₅Au₁-TiO₂. The obtained sample was denoted as E₇-Cu₅Au₁-Al₂O₃.

Synthesis of C₃N₄

C₃N₄ was prepared by polymerization method. 10 g of melamine powder was dispersed into 50 mL of deionized aqueous solution and kept in an ultrasonic bath for 30 min. The mixture was stirred in water bath at 50 °C, and then dried in oven at 60 °C. The as-prepared powder was grounded, and then transferred into ceramic crucible calcined at

300 °C for 1 h, 400 °C for 1 h, and 550 °C for 4 h with 2.5 °C·min⁻¹ heating rate in a muffle furnace. After natural cooling to room temperature, the samples were washed by DI water for three times to remove impurity.

Synthesis of Cu₅Au₁-C₃N₄

Cu₅Au₁-C₃N₄ was prepared by the same approach as Cu₅Au₁-TiO₂, except that the TiO₂ was replaced by C₃N₄.

Synthesis of E_t-Cu₅Au₁-C₃N₄

E_t-Cu₅Au₁-C₃N₄ was prepared by the same approach as E_t-Cu₅Au₁-TiO₂, except that the Cu₅Au₁-TiO₂ was replaced by Cu₅Au₁-C₃N₄.

Characterizations

TEM and EDS mapping analysis (Talos F200X G2 200KV) were applied to confirm the morphologies of the materials. AC-HAADF-STEM was conducted on Titan Cubed Themis G2300 and JEM-ARM200F. XAFS of the Cu K-edge and Au L-edge were measured at the BL14W1 station of the Shanghai Synchrotron Radiation Facility (SSRF, China), and Cu foil and Au foil were used as the reference samples. XAFS data were obtained by means of Athena and Artemis software according to standard procedures. ICP-AES was carried out on a Varian VISTA-MPX instrument. The crystal structure was characterized by powder XRD using Cu K α radiation ($\lambda = 0.15406$ nm) on a Bruker D8 Advance X-ray diffractometer. The compositions of the catalysts were analyzed by XPS (Thermo Scientific K-Alpha). UV-vis-NIR DRS was performed on a Shimadzu UV-2450 spectrophotometer. PL and TRPL analyses were conducted by means of an Edinburgh Instruments instrument (FLS-980). TPD tests were performed on an AutoChem1 II 2920 with a thermal conductivity detector. The surface hydrophilicity of the as-prepared samples was determined by contact angle measurement (CA, KSV CM200, Finland).

Photoelectrochemical tests

Photocurrent and EIS tests were conducted by a CHI660B electrochemical analyzer with a standard three-electrode system, where Ag/AgCl and Pt wire were used as reference and counter electrodes, respectively, and the samples spin-coated onto fluorine-doped tin oxide (FTO) glasses served as working electrodes. During the photocurrent and EIS tests, 0.2 mol·L⁻¹ Na₂SO₄ solution and 0.1 mol·L⁻¹ KCl solution containing 5 mmol·L⁻¹ K₄[Fe(CN)₆]/K₃[Fe(CN)₆] were applied as electrolytes. Moreover, the Mott-Schottky test was carried out in a 0.5 mol·L⁻¹ Na₂SO₄ solution.

Photocatalytic activity tests in different reaction systems

(a) Static system: 20 mg of photocatalyst and 5 mL of deionized water were dispersed on a 45 mm diameter quartz glass under sonication and then placed at 60 °C in a vacuum oven for 3 h to dry. Photoreduction CO₂ reaction tests were conducted on a closed glass gas-circulation system (Labsolar-6A, Beijing Perfectlight Technology Co., Ltd) with the addition of 2 mL deionized water, and a quartz tray was used to separate water and the quartz glass coated by photocatalysts. The temperature was adjusted to 25 °C using circulating water. (b) intermittent flow system: 2.0 mg of photocatalyst was dispersed on the surface of the microporous membrane with a radius of 2.35 cm by filtration and then sealed in the intermittent flow system with the addition of 0.5 mL deionized water. Before irradiation, the gas-circulation system was vacuum-treated for 15 min and then filled with high-purity CO₂ (99.99%). The reactor filled with high-purity CO₂ was vacuum-treated again and then filled with high-purity CO₂ to reach 90 kPa. The photocatalyst was placed 10 cm away from a 300 W Xe lamp (Microsolar 300, 320–780 nm, 250 mW·cm⁻², Beijing Perfectlight Technology Co., Ltd). Gas products were detected by means of a gas chromatograph (GC9790II, FULI INSTRUMENTS) equipped with a flame ionization detector (FID) and thermal conductivity detector (TCD). The produced

gases were calibrated with a standard gas mixture, and the identity was determined by the retention time. ¹³CO₂ isotope labeling experiments were conducted under the same conditions.

¹³CO₂ isotope labeling experiments

The gas products of ¹³CO₂ isotope labeling experiments were conducted on Agilent 7890B-5977B GC with MS detector. The HP-5MS type column was adopted to analyze the C-based products. The heating programming was started at 40 °C and maintained for 5 min. The temperature of system was increasing from 40 °C to 290 °C with a heating rate of 20 °C·min⁻¹, and the system kept 290 °C for 10 min. Helium was used as a carrier gas in GC with a flow rate of 1 mL·min⁻¹. The temperature of gas sampling valve is 280 °C under non-diversion mode. Electron impact ionization with 70 eV voltage under the full scan of 2-350 u. The matching degree of CO, CH₄, C₂H₄, and C₂H₆ relied on the database are about 93, 96, 92, and 93%, respectively, which could be regarded as the reference for source of C-based products.

In situ DRIFTS experiments

In situ DRIFTS experiments were conducted on a Nicolet iS10 (Thermo) machine, and the photocatalysts were sealed in the reaction chamber with a quartz window. CO₂ and H₂O were carried into the reaction chamber by N₂ flow until equilibrium. After taking the equilibrium system before reaction as the blank background, IR signals were collected under 355 nm laser irradiation (3W) through the quartz glass window.

XAFS data analysis

Data reduction, data analysis, and EXAFS fitting were performed and analyzed with the Athena and Artemis programs of the Demeter data analysis packages¹⁰³ that utilizes the FEFF6 program¹⁰⁴ to fit the EXAFS data. The energy calibration of the sample was conducted through a standard Cu foil, which as a reference was simultaneously measured. A linear function was subtracted from the pre-edge region, then the edge jump was normalized using Athena software. The k³-weighted $\chi(k)$ data were Fourier transformed after applying a Kaiser-Bessel window function ($\Delta k = 1.0$). For EXAFS modeling, the global amplitude EXAFS (CN , R , σ^2 and ΔE_0) were obtained by nonlinear fitting, with least-squares refinement, of the EXAFS equation to the Fourier-transformed data in R-space, using Artemis software, EXAFS of the Cu foil is fitted and the obtained amplitude reduction factor S_0^2 value (0.845) was set in the EXAFS analysis to determine the coordination numbers (CNs) in the Cu-O and Cu-Au scattering path in sample.

Computational methods

DFT models were constructed based on the results of AC-HAADF-STEM and XRD, and the (101) crystal plane of TiO₂ was selected to construct the computational models. All DFT calculations were performed by the Vienna Ab Initio Simulation Package (VASP). The Perdew-Burke-Ernzerhof (PBE) generalized gradient approximation (GGA) was utilized to address the exchange-correlation interactions. All slab models were applied with a 15 Å vacuum layer to prevent interactions between slabs. A 2 × 2 × 1 k-point was sampled in the Brillouin zone. A plane-wave basis expansion with a 400 eV energy cutoff was adopted to optimize the geometric structures, and the electronic forces were converged to 1 × 10⁻⁵ and 0.03 eV·Å⁻¹, respectively. The Gibbs free energies were calculated at 298.15 K by means of the formula $G = E_{\text{DFT}} - TS + E_{\text{ZPE}}$, where E_{DFT} , TS , and E_{ZPE} represent the electronic energy of each step, entropy contribution, and zero-point energy, respectively.

Data availability

All data that support the findings of this study are present in the paper and the Supplementary Information. Further information can be

acquired from the corresponding authors. Source data are provided with this paper.

References

- Peter, S. C. Reduction of CO₂ to chemicals and fuels: a solution to global warming and energy crisis. *ACS Energy Lett.* **3**, 1557–1561 (2018).
- Gao, W. L. et al. Industrial carbon dioxide capture and utilization: state of the art and future challenges. *Chem. Soc. Rev.* **49**, 8584–8686 (2020).
- Albero, J., Peng, Y. & Garcia, H. Photocatalytic CO₂ reduction to C₂₊ products. *ACS Catal.* **10**, 5734–5749 (2020).
- Gao, W. et al. Vacancy-defect modulated pathway of photo-reduction of CO₂ on single atomically thin AgInP₂S₆ sheets into olefiant gas. *Nat. Commun.* **12**, 4747 (2021).
- Shao, W. et al. Metal⁰-Metal^{δ+} pair sites steer C–C coupling for selective CO₂ photoreduction to C₂ hydrocarbons. *Nano Res.* **15**, 1882–1891 (2022).
- Wang, W. et al. Photocatalytic C–C coupling from carbon dioxide reduction on copper oxide with mixed-valence copper(I)/copper(II). *J. Am. Chem. Soc.* **143**, 2984–2993 (2021).
- Wang, T. et al. Engineering catalytic interfaces in Cu^{δ+}/CeO₂-TiO₂ photocatalysts for synergistically boosting CO₂ reduction to ethylene. *ACS Nano* **16**, 2306–2318 (2022).
- Tian, F. Y. et al. Visible-light-driven CO₂ reduction to ethylene on CdS: enabled by structural relaxation-induced intermediate dimerization and enhanced by ZIF-8 coating. *Appl. Catal. B Environ.* **285**, 119834 (2021).
- Xie, W. K. et al. P-mediated Cu-N₄ sites in carbon nitride realizing CO₂ photoreduction to C₂H₄ with selectivity modulation. *Adv. Mater.* **35**, 2208132 (2022).
- Chakraborty, S. et al. Wurtzite CuGaS₂ with an in-situ-formed CuO layer photocatalyzes CO₂ conversion to ethylene with high selectivity. *Angew. Chem. Int. Ed.* **63**, e202216613 (2023).
- Kou, M. P. et al. Photocatalytic CO₂ conversion over single-atom MoN₂ sites of covalent organic framework. *Appl. Catal. B: Environ.* **291**, 120146 (2021).
- Das, R. et al. Engineering the charge density on an In_{2.77}S₄/porous organic polymer hybrid photocatalyst for CO₂-to-ethylene conversion reaction. *J. Am. Chem. Soc.* **145**, 422–435 (2023).
- Hao, J. X. et al. Utilizing new metal phase nanocomposites deep photocatalytic conversion of CO₂ to C₂H₄. *Chem. Eng. J.* **423**, 130190 (2021).
- Wu, Z. Z. et al. Identification of Cu(100)/Cu(111) interfaces as superior active sites for CO dimerization during CO₂ electro-reduction. *J. Am. Chem. Soc.* **144**, 259–269 (2022).
- Jouny, M., Hutchings, G. S. & Jiao, F. Carbon monoxide electro-reduction as an emerging platform for carbon utilization. *Nat. Catal.* **2**, 1062 (2019).
- Wang, Y. H., Liu, J. L. & Zheng, G. F. Designing copper-based catalysts for efficient carbon dioxide electroreduction. *Adv. Mater.* **33**, 2005798 (2021).
- Dinh, C. et al. CO₂ electroreduction to ethylene via hydroxide-mediated copper catalysis at an abrupt interface. *Science* **360**, 783–787 (2018).
- Lum, Y. W. & Ager, J. W. Sequential catalysis controls selectivity in electrochemical CO₂ reduction on Cu. *Energy Environ. Sci.* **11**, 2935 (2018).
- Zhu, J. B. et al. Quasi-covalently coupled Ni–Cu atomic pair for synergistic electroreduction of CO₂. *J. Am. Chem. Soc.* **144**, 9661–9671 (2022).
- Chen, S. F. et al. Engineering support and distribution of palladium and tin on MXene with modulation of the d-band center for CO-resilient methanol oxidation. *Angew. Chem. Int. Ed.* **61**, e202209693 (2022).
- Zhong, D. Z. et al. Coupling of Cu(100) and (110) facets promotes carbon dioxide conversion to hydrocarbons and alcohols. *Angew. Chem. Int. Ed.* **60**, 4879–4885 (2021).
- Wu, Y. et al. Selective CO₂-to-C₂H₄ photoconversion enabled by oxygen-mediated triatomic sites in partially oxidized bimetallic sulfide. *Angew. Chem. Int. Ed.* **62**, e202301075 (2023).
- Yan, K. et al. Highly selective ethylene production from solar-driven CO₂ reduction on the Bi₂S₃@In₂S₃ catalyst with In–S_v–Bi active sites. *ACS Catal.* **13**, 2302–2312 (2023).
- Wang, J. Y. et al. Regulating the metallic Cu–Ga bond by S vacancy for improved photocatalytic CO₂ reduction to C₂H₄. *Adv. Funct. Mater.* **33**, 2213901 (2023).
- Zeng, D. et al. Photocatalytic conversion of CO₂ to acetic acid by CuPt/WO₃: chloride enhanced C–C coupling mechanism. *Appl. Catal. B* **323**, 122177 (2023).
- Huang, F. et al. Low-temperature acetylene semi-hydrogenation over the Pd₁-Cu₁ dual-atom catalyst. *J. Am. Chem. Soc.* **144**, 18485–18493 (2022).
- Hai, X. et al. Geminal-atom catalysis for cross-coupling. *Nature* **622**, 754–760 (2023).
- Wang, L. L., Wang, H. W. & Lu, J. L. Local chemical environment effect in single-atom catalysis. *Chem. Catal.* **3**, 100492 (2023).
- Hu, B. et al. Atomic Co/Ni dual sites with N/P coordination as bifunctional oxygen electrocatalyst for rechargeable zinc-air batteries. *Nano Res.* **14**, 3482–3488 (2021).
- Wan, W. et al. Mechanistic insight into the active centers of single/dual-atom Ni/Fe-based oxygen electrocatalysts. *Nat. Commun.* **12**, 5589 (2021).
- Sours, T. et al. Circumventing scaling relations in oxygen electrochemistry using metal-organic framework. *J. Phys. Chem. Lett.* **11**, 10029–10036 (2020).
- Yi, J. D. et al. Design of Co–Cu diatomic site catalysts for high-efficiency synergistic CO₂ electroreduction at industrial-level current density. *Angew. Chem. Int. Ed.* **61**, e202212329 (2022).
- Liang, Z. et al. Tunable CO/H₂ ratios of electrochemical reduction of CO₂ through the Zn–Ln dual atomic catalysts. *Sci. Adv.* **7**, eabl4915 (2021).
- Hao, J. C. et al. Interatomic electronegativity offset dictates selectivity when catalyzing the CO₂ reduction reaction. *Adv. Energy Mater.* **12**, 2200579 (2022).
- Shi, H. N. et al. Atomically dispersed indium-copper dual-metal active sites promoting C–C coupling for CO₂ photoreduction to ethanol. *Angew. Chem. Int. Ed.* **61**, e202208904 (2022).
- Coperet, C. et al. Surface organometallic and coordination chemistry toward single-site heterogeneous catalysts: strategies, methods, structures, and activities. *Chem. Rev.* **116**, 323–421 (2016).
- Delley, M. F. et al. Local structures and heterogeneity of silica-supported M(III) sites evidenced by EPR, IR, NMR, and luminescence spectroscopies. *J. Am. Chem. Soc.* **139**, 8855–8867 (2017).
- Merle, N. et al. Well-defined molybdenum oxo alkyl complex supported on silica by surface organometallic chemistry: a highly active olefin metathesis precatalyst. *J. Am. Chem. Soc.* **139**, 2144–2147 (2017).
- Wei, H. S. et al. FeO_x-supported platinum single-atom and pseudo-single-atom catalysts for chemoselective hydrogenation of functionalized nitroarenes. *Nat. Commun.* **5**, 5634–5641 (2014).
- Lin, J. et al. Remarkable performance of Ir₁/FeO_x single-atom catalyst in water gas shift reaction. *J. Am. Chem. Soc.* **135**, 15314–15317 (2013).
- Zhang, B. et al. Stabilizing a platinum₁ single-atom catalyst on supported phosphomolybdic acid without compromising hydrogenation activity. *Angew. Chem. Int. Ed.* **55**, 8319–8323 (2016).
- Li, X. G. et al. Single-atom Pt as co-catalyst for enhanced photocatalytic H₂ evolution. *Adv. Mater.* **28**, 2427–2431 (2016).

43. Yang, S. et al. Support effects in single-atom platinum catalysts for electrochemical oxygen reduction. *ACS Catal.* **7**, 1301–1307 (2017).
44. Sun, J. et al. Diatomic Pd-Cu metal-phosphorus sites for complete N≡N bond formation in photoelectrochemical nitrate reduction. *Angew. Chem. Int. Ed.* **61**, e202211373 (2022).
45. Liu, P. X. et al. Photochemical route for synthesizing atomically dispersed palladium catalysts. *Science* **352**, 797–800 (2016).
46. O'Neill, B. J. et al. Catalyst design with atomic layer deposition. *ACS Catal.* **5**, 1804–1825 (2015).
47. Sun, S. H. et al. Single-atom catalysis using Pt/graphene achieved through atomic layer deposition. *Sci. Rep.* **3**, 1775 (2013).
48. Li, R. Z., Zhao, J., Liu, B. Z. & Wang, D. S. Atomic distance engineering in metal catalysts to regulate catalytic performance. *Adv. Mater.* **36**, 2308653 (2023).
49. Hahn, C., Hatsukade, T., Kim, Y. G. & Jaramillo, T. F. Engineering Cu surfaces for the electrocatalytic conversion of CO₂: controlling selectivity toward oxygenates and hydrocarbons. *Proc. Natl Acad. Sci. USA* **114**, 5918–5923 (2017).
50. Yao, K. L. et al. Mechanistic insights into OC-COH coupling in CO₂ electroreduction on fragmented copper. *J. Am. Chem. Soc.* **144**, 14005–14011 (2022).
51. Zaza, L., Rossi, K. & Buonsanti, R. Well-defined copper-based nanocatalysts for selective electrochemical reduction of CO₂ to C₂ products. *ACS Energy Lett.* **7**, 1284–1291 (2022).
52. Gu, Z. X. et al. Efficient electrocatalytic CO₂ reduction to C₂₊ alcohols at defect-site-rich Cu surface. *Joule* **5**, 429–440 (2021).
53. Vasileff, A. et al. Surface and interface engineering in copper-based bimetallic materials for selective CO₂ electroreduction. *Chem* **4**, 1809–1831 (2018).
54. Wei, T. et al. Facet-regulating local coordination of dual-atom cocatalyzed TiO₂ for photocatalytic water splitting. *ACS Catal.* **11**, 14669–14676 (2021).
55. Tu, W. G. et al. An in situ simultaneous reduction-hydrolysis technique for fabrication of TiO₂-graphene 2D sandwich-like hybrid nanosheets: graphene-promoted selectivity of photocatalytic-driven hydrogenation and coupling of CO₂ into methane and ethane. *Adv. Funct. Mater.* **23**, 1743–1749 (2013).
56. Xiong, X. Y. et al. Photocatalytic CO₂ reduction to CO over Ni single atoms supported on defect-rich zirconia. *Adv. Energy Mater.* **10**, 2002928 (2020).
57. Yu, Y. Y. et al. Synergistic effect of Cu single atoms and Au-Cu alloy nanoparticles on TiO₂ for efficient CO₂ photoreduction. *ACS Nano* **15**, 14453–14464 (2021).
58. Yuan, L. et al. Dynamic evolution of atomically dispersed Cu species for CO₂ photoreduction to solar fuels. *ACS Catal.* **9**, 4824–4833 (2019).
59. Zhang, X. et al. Platinum-copper single atom alloy catalysts with high performance towards glycerol hydrogenolysis. *Nat. Commun.* **10**, 5812 (2019).
60. Xie, Z. K. et al. Construction of CuO quantum dots/WO₃ nanosheets OD/2D Z-scheme heterojunction with enhanced photocatalytic CO₂ reduction activity under visible-light. *J. Alloys Compd* **858**, 157668 (2021).
61. Mansour, A. N. Copper Mg Kα XPS spectra from the physical electronics model 5400 spectrometer. *Surf. Sci. Spectra* **3**, 202–210 (1994).
62. Liu, Q. et al. Vacancy engineering of AuCu cocatalysts for improving the photocatalytic conversion of CO₂ to CH₄. *J. Mater. Chem. A* **7**, 27007–27015 (2019).
63. Li, D. et al. Steering multistep charge transfer for highly selectively photocatalytic reduction of CO₂ into CH₄ over Pd/Cu₂O/TiO₂ ternary hybrid. *Sol. RRL* **5**, 2000813 (2021).
64. Milazzo, G., Caroli, S. & Sharma, V. K. Tables of standard electrode potentials. *J. Electrochem. Soc.* **125**, 261C (1978).
65. Chen, H. Q. et al. Unmasking the critical role of the ordering degree of bimetallic nanocatalysts on oxygen reduction reaction by in Situ raman spectroscopy. *Angew. Chem. Int. Ed.* **61**, e202117834 (2022).
66. Nadeem, M. A. et al. Hydrogen production on Ag-Pd/TiO₂ bimetallic catalysts: is there a combined effect of surface plasmon resonance with Schottky mechanism on the photo-catalytic activity? *ChemistrySelect* **2**, 2754–2762 (2017).
67. Xu, Y. et al. A CsPbBr₃ perovskite quantum dot/graphene oxide composite for photocatalytic CO₂ reduction. *J. Am. Chem. Soc.* **139**, 5660–5663 (2017).
68. Cui, X. et al. Turning Au nanoclusters catalytically active for visible-light driven CO₂ reduction through bridging ligands. *J. Am. Chem. Soc.* **140**, 16514–16520 (2018).
69. Wang, S. et al. Intermolecular cascaded π-conjugation channels for electron delivery powering CO₂ photoreduction. *Nat. Commun.* **11**, 1149 (2020).
70. Kim, D. et al. Synergistic geometric and electronic effects for electrochemical reduction of carbon dioxide using gold-copper bimetallic nanoparticles. *Nat. Commun.* **5**, 4948 (2014).
71. Jiang, D. L. et al. Synergistic integration of AuCu co-catalyst with oxygen vacancies on TiO₂ for efficient photocatalytic conversion of CO₂ to CH₄. *ACS Appl. Mater. Interfaces* **13**, 46772–46782 (2021).
72. Zhao, L. H. et al. Lattice engineering on metal cocatalysts for enhanced photocatalytic reduction of CO₂ into CH₄. *ChemSusChem* **11**, 3524–3533 (2018).
73. Cai, X. T. et al. Order engineering on the lattice of intermetallic PdCu co-catalysts for boosting the photocatalytic conversion of CO₂ into CH₄. *J. Mater. Chem. A* **6**, 17444 (2018).
74. Wang, E. R. Y. et al. Solar-driven photocatalytic reforming of lignocellulose into H₂ and value-added biochemicals. *ACS Catal.* **12**, 11206–11215 (2022).
75. Li, Y. et al. Crystalline carbon nitride supported copper single atoms for photocatalytic CO₂ reduction with nearly 100% CO selectivity. *ACS Nano* **14**, 10552–10561 (2020).
76. Yin, H. B., Dong, F., Wang, D. S. & Li, J. H. Coupling Cu single atoms and phase junction for photocatalytic CO₂ reduction with 100% CO selectivity. *ACS Catal.* **12**, 14096–14105 (2022).
77. Bao, X. L. et al. Molten-salt assisted synthesis of Cu clusters modified TiO₂ with oxygen vacancies for efficient photocatalytic reduction of CO₂ to CO. *Chem. Eng. J.* **445**, 136718 (2022).
78. Wang, Z. W. et al. Cu⁺-Ti³⁺ interface interaction mediated CO₂ coordination model for controlling the selectivity of photocatalytic reduction CO₂. *Appl. Catal. B: Environ.* **301**, 120803 (2022).
79. Huang, G. C. et al. Spatial confinement of copper single atoms into covalent triazine-based frameworks for highly efficient and selective photocatalytic CO₂ reduction. *Nano Res.* **15**, 8001–8009 (2022).
80. Wang, Y. J. & He, T. Recent advances and comprehensive consideration on the oxidation half reaction in photocatalytic CO₂ conversion. *J. Mater. Chem. A* **9**, 87–110 (2021).
81. Wang, H. N. et al. Recent progress and perspectives in heterogeneous photocatalytic CO₂ reduction through a solid-gas mode. *Coord. Chem. Rev.* **438**, 213906 (2021).
82. Fu, J. W. et al. Product selectivity of photocatalytic CO₂ reduction reactions. *Mater. Today* **32**, 222–243 (2020).
83. Ola, O. & Maroto-Valer, M. M. Review of material design and reactor engineering on TiO₂ photocatalysis for CO₂ reduction. *J. Photochem. Photobiol. C* **24**, 16–42 (2015).
84. Liu, B. J. et al. Effect of solvents on photocatalytic reduction of carbon dioxide using TiO₂ nanocrystal photocatalyst embedded in SiO₂ matrices. *J. Photochem. Photobiol. A* **108**, 235–238 (1997).

85. Carroll, J. J. et al. Triphase photocatalytic CO₂ reduction over silver-decorated titanium oxide at a gas-water boundary. *Angew. Chem. Int. Ed.* **61**, e202200802 (2022).
86. Huang, H. M. et al. Triphase photocatalytic CO₂ reduction over silver-decorated titanium oxide at a gas-water boundary. *Angew. Chem. Int. Ed.* **61**, e202200802 (2022).
87. Wang, K., Fu, J. L. & Zheng, Y. Insights into photocatalytic CO₂ reduction on C₃N₄: strategy of simultaneous B, K co-doping and enhancement by N vacancies. *Appl. Catal. B: Environ.* **254**, 270–282 (2019).
88. Li, N. X. et al. Toward high-value hydrocarbon generation by photocatalytic reduction of CO₂ in water vapor. *ACS Catal.* **9**, 5590–5602 (2019).
89. Paul, R. et al. Tweaking photo CO₂ reduction by altering lewis acidic sites in metalated-porous organic polymer for adjustable H₂/CO ratio in syngas production. *Angew. Chem. Int. Ed.* **62**, e202311304 (2023).
90. Chen, L. et al. Dual-single-atom tailoring with bifunctional integration for high-performance CO₂ photoreduction. *Adv. Mater.* **33**, 2105135 (2021).
91. Sheng, J. P. et al. Identification of halogen associated active sites on bismuth-based perovskite quantum dots for efficient and selective CO₂ to-CO photoreduction. *ACS Nano* **14**, 13103–13114 (2020).
92. Si, S. H. et al. Low-coordination single Au atoms on ultrathin ZnIn₂S₄ nanosheets for selective photocatalytic CO₂ reduction towards CH₄. *Angew. Chem. Int. Ed.* **61**, e202209446 (2022).
93. Yin, S. K. et al. Boosting water decomposition by sulfur vacancies for efficient CO₂ photoreduction. *Energy Environ. Sci.* **15**, 1556–1562 (2022).
94. Wuttig, A. et al. Tracking a common surface-bound intermediate during CO₂-to fuels catalysis. *ACS Cent. Sci.* **2**, 522–528 (2016).
95. Wang, G. et al. P and Cu dual sites on graphitic carbon nitride for photocatalytic CO₂ reduction to hydrocarbon fuels with high C₂H₆ evolution. *Angew. Chem. Int. Ed.* **61**, e202210789 (2022).
96. Choi, B. N. et al. An in-situ spectroscopic study on the photochemical CO₂ reduction on CsPbBr₃ perovskite catalysts embedded in a porous copper scaffold. *Chem. Eng. J.* **430**, 132807 (2022).
97. Kim, Y. et al. Time-resolved observation of C-C coupling intermediates on Cu electrodes for selective electrochemical CO₂ reduction. *Energy Environ. Sci.* **13**, 4301–4311 (2020).
98. Zhu, S. Q., Jiang, B., Cai, W. B. & Shao, M. H. Direct Observation on reaction intermediates and the role of bicarbonate anions in CO₂ electrochemical reduction reaction on Cu surfaces. *J. Am. Chem. Soc.* **139**, 15664–15667 (2017).
99. Wang, Y. et al. Synergy between plasmonic and sites on gold nanoparticle-modified bismuth-rich bismuth oxybromide nanotubes for the efficient photocatalytic C-C coupling synthesis of ethane. *J. Colloid Interface Sci.* **616**, 649–658 (2022).
100. Rahaman, M. et al. Solar-driven liquid multi-carbon fuel production using a standalone perovskite-BiVO₄ artificial leaf. *Nat. Energy* **8**, 629–638 (2023).
101. Calle-Vallejo, F. & Koper, M. Theoretical considerations on the electroreduction of CO to C₂ species on Cu(100) electrodes. *Angew. Chem. Int. Ed.* **52**, 7282–7285 (2013).
102. Gunathunge, C. M. et al. Existence of an electrochemically inert CO population on Cu electrodes in alkaline pH. *ACS Catal.* **8**, 7507–7516 (2018).
103. Ravel, B. & Newville, M. ATHENA, ARTEMIS, HEPHAESTUS: data analysis for X-ray absorption spectroscopy using IFEFFIT. *J. Synchrotron Radiat.* **12**, 537 (2005).
104. Zabinsky, S. I. et al. Multiple-scattering calculations of x-ray-absorption spectra. *Phys. Rev. B* **52**, 2995 (1995).

Acknowledgements

This work was supported by the National Natural Science Foundation of China (22225808), Sino-German Cooperation Group Project (GZ1579), National Natural Science Foundation of China (22025506), National Natural Science Foundation of China (22075111), Jiangsu Province Innovation Support Program International Science and Technology Cooperation Project (BZ2022045), the Industry Prospect and Key Core Technology (Competition Project) of Jiangsu Province (BE2019093), and National Science and Technology Major Project of China (2021YFB3500700).

Author contributions

Z.X. and W.S. conceived the project and wrote the manuscript. S.S. pointed and revised the shortage during this work. S.X. and X.Wu designed the synthesis of composite samples. L.L. performed the computational calculation. S.G. dealt with the XANES analysis. D.X., B.M., and T.Z. helped with the data collection and analysis. M.C. and X.Wang oversaw the project. All authors discussed and commented on the manuscript.

Competing interests

The authors declare no competing interests.

Additional information

Supplementary information The online version contains supplementary material available at <https://doi.org/10.1038/s41467-024-46745-3>.

Correspondence and requests for materials should be addressed to Weidong Shi or Shuyan Song.

Peer review information *Nature Communications* thanks the anonymous reviewers for their contribution to the peer review of this work. A peer review file is available.

Reprints and permissions information is available at <http://www.nature.com/reprints>

Publisher's note Springer Nature remains neutral with regard to jurisdictional claims in published maps and institutional affiliations.

Open Access This article is licensed under a Creative Commons Attribution 4.0 International License, which permits use, sharing, adaptation, distribution and reproduction in any medium or format, as long as you give appropriate credit to the original author(s) and the source, provide a link to the Creative Commons licence, and indicate if changes were made. The images or other third party material in this article are included in the article's Creative Commons licence, unless indicated otherwise in a credit line to the material. If material is not included in the article's Creative Commons licence and your intended use is not permitted by statutory regulation or exceeds the permitted use, you will need to obtain permission directly from the copyright holder. To view a copy of this licence, visit <http://creativecommons.org/licenses/by/4.0/>.

© The Author(s) 2024